

Weyl nodes in CeRu_4Sn_6 studied by dynamical mean-field theory

Jorūnas Dobilas^{1,2,*} Martin Braß² Frank T. Ebel² Silke Paschen² and Karsten Held^{2,†}

¹*Department of Functional Materials and Electronics, FTMC, 10257 Vilnius, Lithuania*

²*Institute of Solid State Physics, TU Wien, 1040 Vienna, Austria*

(Dated: July 18, 2025)

The heavy fermion compound CeRu_4Sn_6 has recently shown to exhibit a spontaneous nonlinear Hall effect, indicating its topological nature. This is consistent with the lack of inversion symmetry that allows for the existence of Weyl nodes. Here, we employ density functional theory plus dynamical mean-field theory, which is state-of-the-art for such correlated materials, and study the topology of CeRu_4Sn_6 . We find five inequivalent Weyl nodes of either type I or II, each having sixteen symmetry-related replicas. These Weyl nodes bridge the Kondo insulating gap, which is a direct but not an indirect gap. The closest Weyl points is only 0.5 meV below the Fermi energy, and has a flat energy-momentum dispersion.

I. INTRODUCTION

Quantum materials [1], in particular when hosting non-trivial electronic topology [2–5] are in high demand for new electronic and quantum devices [6, 7]. In strongly correlated electron systems, the interplay of electron interactions and crystalline symmetries gives rise to a rich landscape of emergent quantum phases—including heavy fermion metals, Kondo insulators, and correlation-driven topological semimetals [8, 9]. Their many-body nature makes it challenging to describe them theoretically, yet they offer a fertile ground for developing and testing new approaches.

A recently established strongly correlated topological phase is the Weyl-Kondo semimetal [10–12], with the compound $\text{Ce}_3\text{Bi}_4\text{Pd}_3$ as a first materials’ realization [10, 12, 13]. Here, we study the compound CeRu_4Sn_6 , which crystallizes in a non-centrosymmetric tetragonal crystal structure of the space group $I\bar{4}2m$ (No. 121) [14]. Early electrical resistivity [15], optical conductivity data [16] on single crystals, and NMR data on powder [17] led to the interpretation of CeRu_4Sn_6 as a “failed” Kondo insulator: With decreasing temperature, a Kondo insulator gap starts to form but ultimately fails to develop fully, leading to a semimetallic ground state. Later, from a treatment using density functional theory (DFT) plus the Gutzwiller approximation, it was proposed that CeRu_4Sn_6 might be a correlated Weyl semimetal [18]. Most recently, the hallmark of a strongly correlated Weyl semimetal—a spontaneous nonlinear Hall effect [12, 19]—was indeed identified in low-temperature experiments on CeRu_4Sn_6 [20]. Furthermore, the electronic specific heat was understood as a convolution of a quantum critical contribution that dominates at high temperatures and a T^3 contribution that evidences the linear Weyl dispersion, with extremely small Weyl velocity, at low temperatures [20]. Motivated by these findings, we here investigate the situation from a DFT plus dynamical mean field

theory (DMFT) [21–25] perspective.

In DMFT, the complex many-body problem is mapped onto an effective Anderson impurity model that is solved self-consistently [22, 23]. This captures the local electronic correlations of the Ce $4f$ electrons while preserving the initial character of the conduction electrons. The combined DFT+DMFT [26–28] approach enables the extraction of momentum-resolved spectral functions, self-energies, and renormalized bands for real materials [25, 28]. Furthermore, it is possible to extract topological features from the renormalized band structures, such as Weyl points or surface states for finite-volume systems.

In the present paper, we employ this DFT+DMFT approach and a search algorithm that follows the Berry curvature to the Weyl nodes. We find that the hybridization between Ce $4f$ and conduction electrons leads to a direct (but not indirect) gap throughout the Brillouin zone. This direct gap is bridged along some low symmetry directions by $5 \times 16 = 80$ Weyl nodes.

The paper is organized as follows: In Section II we briefly recapitulate the computational methods used, i.e., the DFT+DMFT approach in Section II A and the Weyl node search algorithm in Section II B. In Section III we present the results obtained starting with the DFT+DMFT spectra and self energies in Section III A before turning to the topological properties in Section III B. Section IV summarizes our results; and Appendix A lists the symmetry operations for obtaining all 80 Weyl nodes from the five inequivalent ones.

II. COMPUTATIONAL DETAILS

A. DFT+DMFT

As a first step of our DFT+DMFT study, the electronic band structure of CeRu_4Sn_6 is calculated using the (FPLO) code [29] and, for comparison, the WIEN2K [30] full potential linearized augmented plane wave (FP-LAPW) package. Details of the crystal structure of CeRu_4Sn_6 [14] are summarized in Fig. 1. Following previous studies [18, 31], we calculate the electronic

* jorunas.dobilas@ftmc.lt

† held@iftuwien.ac.at

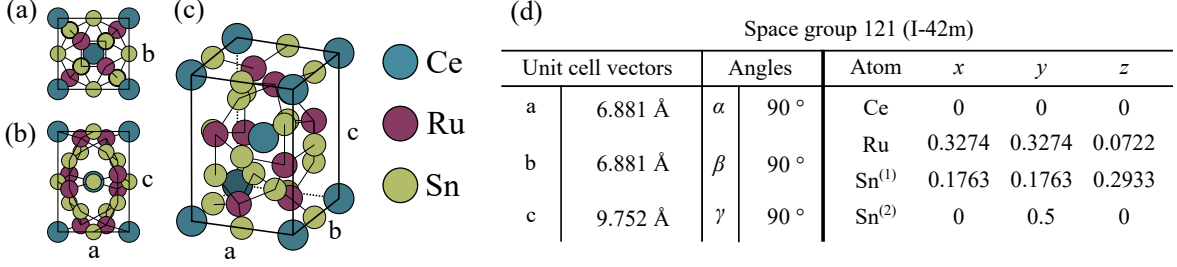


FIG. 1. Crystal structure of CeRu₄Sn₆. (a) and (b) show projections of the crystal structure along the (001) and (010) directions, respectively, (c) a three-dimensional view of the unit cell. In (d), the atomic coordinates are expressed in units of the lattice vectors. The crystallographic parameters are taken from [14].

band structure using the local density approximation (LDA) with the Perdew-Wang exchange-correlation potential [32] and a dense ($6 \times 6 \times 6$) \mathbf{k} mesh to determine the electronic band structure. After the calculation converges, we take the resulting ground state density as the starting point for another self-consistent computation, where we increase the \mathbf{k} mesh to ($12 \times 12 \times 12$). This computation converges immediately, which confirms that the initial \mathbf{k} mesh is sufficient. All calculations are fully relativistic, especially including spin-orbit coupling (SOC).

To simplify our DMFT calculations and to improve numerical accuracy, we employ a tight-binding Hamiltonian based on the FPLO calculation. The tight-binding parameterization is motivated by the fact that subsequent calculations involve extensive sampling at different \mathbf{k} points, where the reduced basis significantly improves computational efficiency. The new basis consists of 90 orbitals, giving a 90×90 Hamiltonian matrix. These orbitals are

- Ce $4f$ orbitals (total of 14: 6 $f_{5/2}$ and 8 $f_{7/2}$ orbitals),
- Ru $4d$ orbitals (total of $4 \cdot 10 = 40$: 4 \cdot 6 $d_{5/2}$ and 4 \cdot 4 $d_{3/2}$ orbitals),
- Sn $5p$ orbitals (total of $6 \cdot 6 = 36$ orbitals: 6 \cdot 4 $p_{3/2}$ and 6 \cdot 2 $p_{1/2}$ orbitals).

The energy range spanned by all orbitals extends from -5 eV to 5 eV, which is sufficient to capture the relevant electronic behavior near the Fermi level.

Subsequent DMFT calculations are performed using the open-source code w2DYNAMICS [33], with continuous-time quantum Monte Carlo (QMC) in the hybridization expansion [34] as a DMFT impurity solver. The schematic diagram for the DMFT self-consistency cycle is presented in Fig. 2. The Hamiltonian solved in DMFT consists of the aforementioned tight-binding Hamiltonian and a Coulomb interaction for the Ce $4f_{5/2}$ manifold. The Ce $4f_{7/2}$ bands are above the Fermi energy, which justifies treating the interaction in a static way as a Hartree-like shift. The intraorbital (U) and interorbital (V) Coulomb interaction potentials are set to the same

value of 5.5 eV for the Ce $4f_{5/2}$ bands, consistent with values used in the literature [31]. Additionally, the Hund's coupling is set to zero, which is justified to some extent by the fact that Ce is in a $4f^1$ configuration. Hence, the Hund's exchange is only relevant for excited states and multiplet admixing. To avoid double counting correlation effects that are partially included in the DFT functional, these are subtracted using the Anisimov formula $V_{DC} = U(\langle n \rangle - \frac{1}{2})$ [35]. For CeRu₄Sn₆, with a Ce $4f$ shell filling of $\langle n \rangle \approx 0.73$ from DFT calculations, this correction is $V_{DC} = 1.27$ eV.

The DMFT loop is iterated for 10 self-consistency steps. In each step, 2×10^8 QMC warm-up and 10^7 measurement sweeps are performed. This procedure is independently repeated at multiple temperatures T to capture the thermal evolution of the correlated electronic structure. The calculations are in the paramagnetic phase, which correctly captures the experimental situation [20]. After completion of the DMFT iterations, we obtain Green's functions $G(i\omega_n)$ and self-energies $\Sigma(i\omega_n)$ at Matsubara frequencies $i\omega_n = (2n + 1)\pi/\beta$ for the correlated Ce $4f_{5/2}$ orbitals. These are then analytically continued to real frequencies ω using the open-source maximum entropy analytical continuation package ANA_CONT [36]. The spectral function $A(\omega)$ is connected to $G(\omega)$ through the relation $A(\omega) = -\frac{1}{\pi} \text{Im}G(\omega)$.

To represent the many-body effects of DMFT, we further employ a quasiparticle renormalization of the DFT bands by expanding Green's functions around the Fermi level. The quasiparticle weight Z for the different Ce $4f_{5/2}$ states is calculated from the real part of the self-energy:

$$Z = \left(1 - \left. \frac{\partial \text{Re}\Sigma(\omega)}{\partial \omega} \right|_{\omega=0} \right)^{-1}. \quad (1)$$

The quasiparticle representation then yields the renormalized Hamiltonian matrix

$$H_{qp}(\mathbf{k}) = \sqrt{Z} (H(\mathbf{k}) + \text{Re}\Sigma(0) - \mu\mathbb{I} - V_{DC}) \sqrt{Z}. \quad (2)$$

Here $H(\mathbf{k})$ is the original tight-binding Hamiltonian matrix; \mathbb{I} the identity matrix; Z , $\text{Re}\Sigma(0)$ and V_{DC} are in (diagonal) matrix form and have non-zero elements only

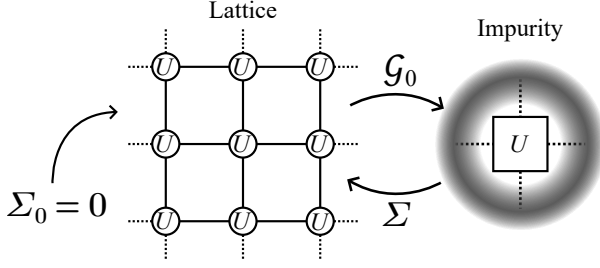


FIG. 2. Self-consistency cycle of dynamical mean-field theory. The lattice model (left) is computed using the initial self-energy $\Sigma_0 = 0$ with on-site Coulomb potential U . The dynamic Weiss field (G_0) is then extracted from the lattice model and used as input in the Anderson impurity model (right), from which the local self-energy Σ is obtained. This self-energy is then used in turn as input in the lattice model to update G_0 . The cycle is repeated until the convergence of the self-energy is achieved.

for the Ce $4f_{5/2}$ manifold. Using $H_{\text{qp}}(\mathbf{k})$, the quasiparticle Green's function

$$G_{\text{qp}}(\omega, \mathbf{k}) = Z \cdot [\omega - H_{\text{qp}}(\mathbf{k})]^{-1} \quad (3)$$

is then used to compute \mathbf{k} -resolved quasiparticle spectral functions, and to determine the topology of the DFT+DMFT electronic structure.

B. Weyl node search algorithm

An important quantity defining the Weyl nodes is the Berry curvature $\Omega_n(\mathbf{k})$, which characterizes the geometrical structure of Bloch bands. For a given band n , the Berry curvature is defined as a curl of the Berry connection $\mathbf{A}_n(\mathbf{k})$ [37]:

$$\Omega_n(\mathbf{k}) = \nabla \times \mathbf{A}_n(\mathbf{k}), \quad (4)$$

with

$$\mathbf{A}_n(\mathbf{k}) = i \langle u_{n\mathbf{k}} | \nabla_{\mathbf{k}} | u_{n\mathbf{k}} \rangle. \quad (5)$$

Here $u_{n\mathbf{k}}$ is the periodic part of the Bloch function for the n -th band. The topological “charge” of the Weyl nodes is defined by the Chern number, which is computed by integrating $\Omega_n(\mathbf{k})$ over a closed surface S :

$$C_n = \frac{1}{2\pi} \oint_S \Omega_n(\mathbf{k}) d\mathbf{S}. \quad (6)$$

Weyl nodes come in pairs, characterized by their Chern numbers C_n : +1 for a source and -1 for a sink of the Berry curvature $\Omega_n(\mathbf{k})$ in \mathbf{k} space. This behavior is analogous to magnetic monopoles or electric charges in real space.

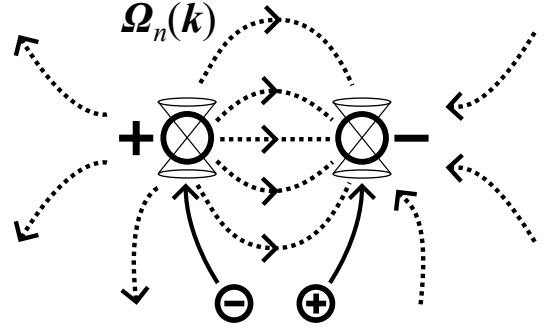


FIG. 3. Schematic representation of the Weyl node search algorithm [38]. Randomly placed “particles” with Chern positive or negative “charges” (\oplus , \ominus) are created and follow the Berry curvature “field lines” $\Omega_n(\mathbf{k})$ (dotted lines) toward the Weyl points (symbolized by a circle with a cone dispersion). Depending on the “charge” of the “particles”, the “charges” will move towards Weyl nodes with Chern numbers +1 or -1, respectively.

There are various methods to find Weyl nodes. The brute-force approach is to take the full lattice cell, subdivide it into smaller pieces, and compute the Berry flux in each cell. If they are small enough to have only one Weyl node per cell, it is possible to pin-point the location of these nodes by continuously making the cells smaller. However, this method is numerically demanding, especially if the nodes are relatively close to each other. We used a more efficient method that is visualized in Fig. 3 and is available as part of the *TightBindingToolBox* [38]. It has been employed successfully to identify Weyl points in the heavy fermion compound $\text{Ce}_3\text{Bi}_4\text{Pd}_3$ [13]. The locations of the Weyl nodes are obtained by introducing particles with Chern “charge” at random starting points in the Brillouin zone, which then follow the Berry curvature. Depending on this “charge”, the particles will approach the nodes with either $C_n = +1$ or $C_n = -1$. This resembles the motion of charged test particles toward an opposite charge at a fixed position. In this way, it is possible to obtain the accurate locations of the Weyl nodes at much lower computational costs.

III. RESULTS

A. DFT+DMFT calculations

Fig. 4 shows the DMFT-computed spectral functions for the Ce $f_{5/2}$ orbitals at three different temperatures: 290 K, 97 K, and 23 K. As the temperature decreases, a spectral peak develops at the Fermi energy and strongly increases in height for the $m_j = \pm 3/2, \pm 1/2$ components; see panels (e) and (f). This behavior is characteristic of the gradual formation of the Kondo resonance at low temperatures, which in our case is saturated at 23 K [the spectral function at 50 K (not shown) is essentially the same as for 23 K.]. In contrast, the $m_j = \pm 5/2$

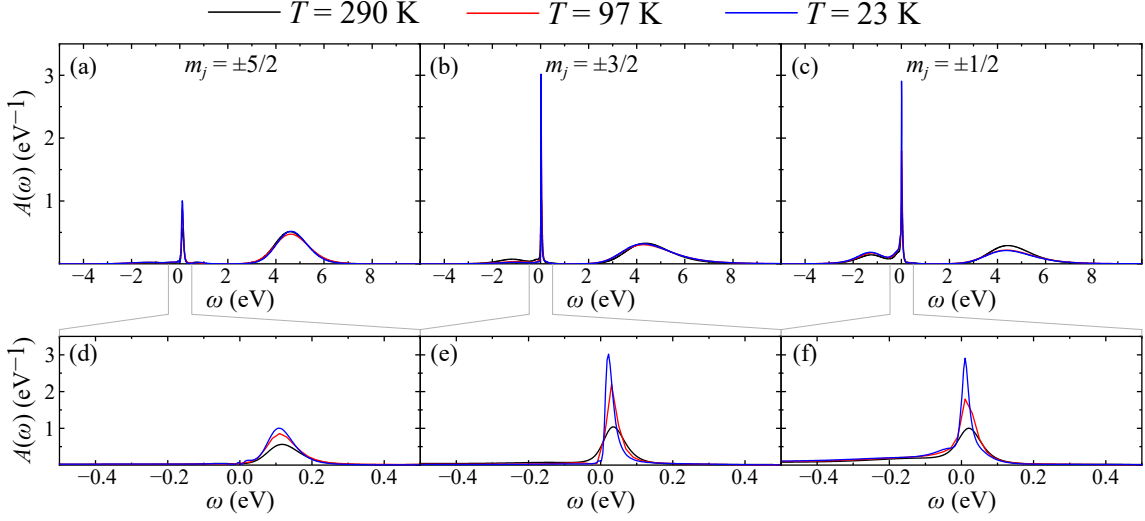


FIG. 4. DMFT spectral functions $A(\omega)$ for the 3×2 Ce $f_{5/2}$ states at three different temperatures: $T = 290$ K (black), $T = 97$ K (red), $T = 23$ K (blue). Results are resolved by total angular momentum projections: $m_j = \pm 5/2$ (a,d), $m_j = \pm 3/2$ (b,e) and $m_j = \pm 1/2$ (c,f). Graphs (a-c) show the full energy range, while (d-f) are zoomed-in views near the Fermi energy.

components exhibit a significantly weaker temperature dependence, showing only minor changes in the studied energy range of panel (a) and (d).

Fig. 5 presents the real and imaginary parts of the self-energy for different m_j projections of the Ce $j = 5/2$ manifold. At room temperature, each m_j component shows different intensities and pole positions. The latter correspond to a (damped) $1/\omega$ behavior of the real part of the self-energy in panel (a), and a maximum in the imaginary part in panel (c). Fig. 5(c). These poles split off the Hubbard bands from the quasiparticle band, and are more pronounced for $\omega > 0$, where the splitting between the quasiparticle band and upper Hubbard band is larger (which requires a larger prefactor of the $1/\omega$ pole). The $m_j = \pm 1/2$ component exhibits minor glitches near $\omega = 0$, which likely arise from numerical artifacts in the analytic continuation.

At lower temperatures (23 K), the pole of $\Sigma(\omega)$ for $m_j = \pm 1/2$ is shifted to higher energies in panel (b), and the region where $\text{Im}\Sigma(\omega)$ is small around the Fermi energy becomes wider in panel (d). This indicates enhanced quasiparticle lifetimes, concomitant with the development of a sharp Kondo resonance. The self-energy of the other orbitals ($m_j = \pm 5/2, \pm 3/2$) becomes nearly degenerate at lower temperatures.

From the DMFT self-energy, we compute Z and $\text{Re}\Sigma(0)$ for each m_j projection of the Ce $4f_{5/2}$ manifold at two temperatures: 290 K and 23 K. For the results, see Table I. In all cases Z remains similar and approximately 0.1. On the other hand, $\text{Re}\Sigma(0)$ is nearly temperature independent for the $m_j = \pm 1/2$ bands, while it is largest for the $m_j = \pm 5/2$ manifold. For $m_j = \pm 3/2, \pm 5/2$, $\text{Re}\Sigma(0)$ becomes smaller as the temperature is reduced. Also shown in Table I is the occupation of these different $4f$ orbitals. With lowering temperature, we see that

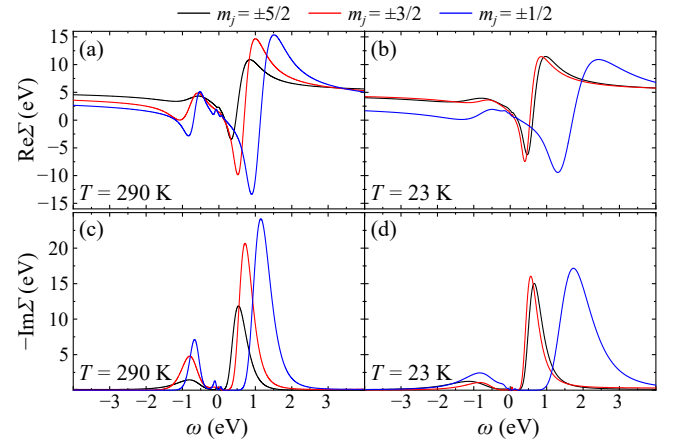


FIG. 5. Real (a,b) and imaginary (c,d) parts of the DMFT self-energy $\Sigma(\omega)$ at two different temperatures: 290 K (a,c), and 23 K (b,d). Results are resolved for different m_j of the Ce $f_{5/2}$ manifold.

the $m_j = \pm 1/2$ occupation increases towards half-filling, whereas the other orbitals depopulate. This agrees with previous DFT+DMFT calculations at higher temperatures [31] and x-ray spectroscopy [39].

Fig. 6 shows the \mathbf{k} -resolved spectral function at 290 K and 23 K. The original DFT bands are overlaid and describe a gapped insulator. Importantly, they fail to describe the correlated spectral function $A(\omega, \mathbf{k})$ around the Fermi energy. This is because they lack the Kondo resonance (or quasiparticle peak). In contrast, the overlaid renormalized quasiparticle bands provide a reliable representation of the many-body spectral function at low energies.

TABLE I. Calculated quasiparticle parameters and electron filling for the full Ce $f_{5/2}$ manifold from DMFT calculations at two different temperatures: 290 K and 23 K. Chemical potential μ is for the 90 orbital basis set.

T , K	m_j	μ , eV	Z	$\text{Re } \Sigma(0)$, eV	$\langle n \rangle$
290	$\pm 1/2$	-0.080	0.1321	0.9514	0.569
	$\pm 3/2$		0.1073	1.3362	0.293
	$\pm 5/2$		0.1261	2.2173	0.096
23	$\pm 1/2$	-0.059	0.1123	1.0125	0.734
	$\pm 3/2$		0.1035	1.2570	0.095
	$\pm 5/2$		0.1228	1.7535	0.107

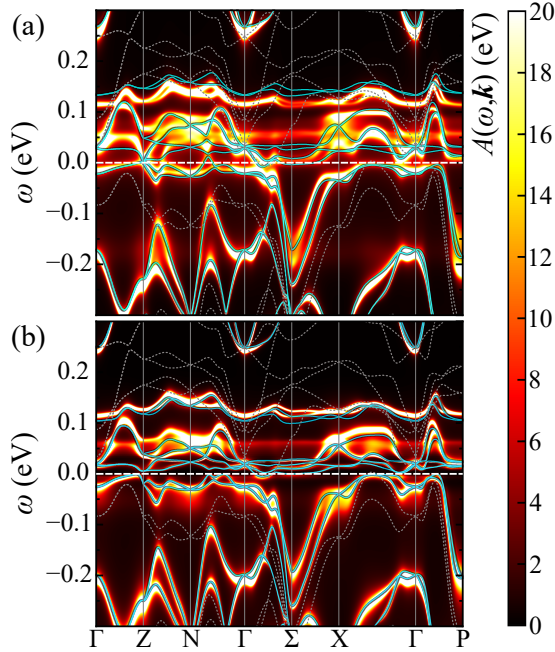


FIG. 6. Total DMFT spectral function $A(\omega, \mathbf{k})$ of all bands at (a) 290 K and (b) 23 K. Overlaid white dashed lines are the initial DFT bands; blue solid lines are the renormalized quasiparticle bands. The latter are in good agreement with the DMFT $A(\omega, \mathbf{k})$ around the Fermi energy.

At $T = 23$ K (Fig. 6(b)), within the low-energy quasiparticle band, a direct gap of ~ 5 meV appears at most wave vectors across the Brillouin zone, in excellent agreement with experiments [17]. This gap becomes visible only at low temperatures where lifetimes are long enough so that the resolution of the bands improves. The reason for the gap opening is the hybridization of the Ce $4f$ states with the conduction bands—the hallmark of a Kondo insulator. However, because the gap is very small and the bands disperse, no indirect band gap forms across the entire Brillouin zone. From Fig. 6, as well as the m_j -resolved spectrum in Fig. 7, it can be seen that there are bands that cross the Fermi energy.

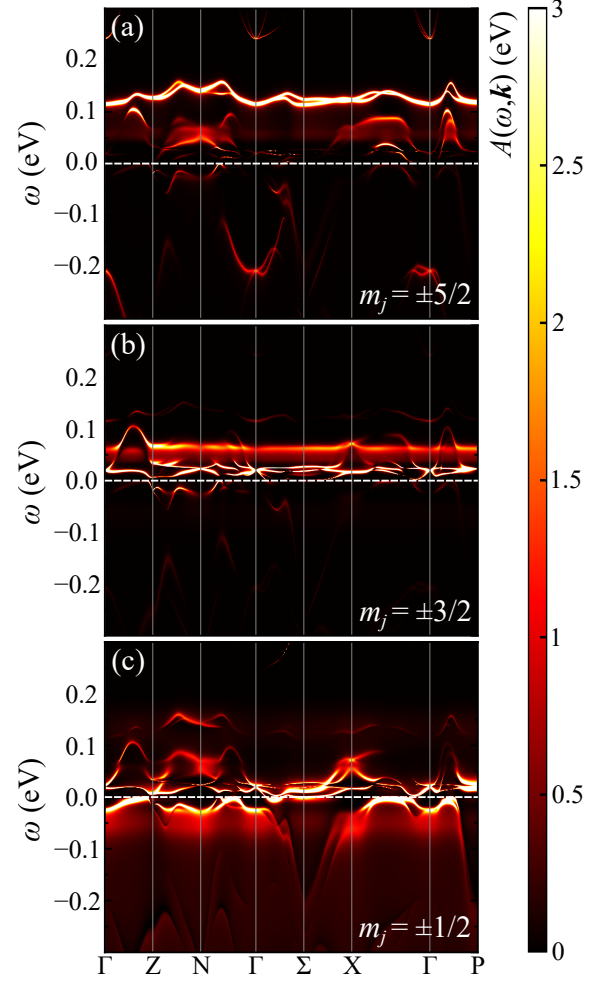


FIG. 7. Contribution of the different Ce $4f_{5/2}$ orbitals to the spectral functions at 23 K: $m_j = \pm 5/2$ (a), $m_j = \pm 3/2$ (b) and $m_j = \pm 1/2$ (c).

As we will show in Fig. 9 below, electronic correlations further lead to topological band crossings of the Kondo insulator direct gap, with a linear dispersion around the Weyl points. Note that in Ref. [31], which used Hirsch-Fye QMC as the DMFT impurity solver, such low temperatures could not be reached. The use of continuous-time QMC is thus essential for the advance presented here.

B. Topological analysis

A search for Weyl nodes in CeRu_4Sn_6 at the Fermi level was carried out using the Weyl node search algorithm of [38]. We focus on the physically most relevant Ce $4f_{5/2}$ orbital with $m_j = (-)1/2$ and used the renormalized quasiparticle Hamiltonian (2) with DMFT self-energy at $T = 23$ K as input. Additionally, FPLO generated primitive unit cell was used. In total, we identified

TABLE II. Coordinates of the inequivalent Weyl nodes in momentum space of a primitive unit cell (normalized by reciprocal lattice vectors $2\pi/a_i$), their type and energies. Here nodes with Chern number +1 are shown, others can be obtained by symmetry transformations (see Appendix A). Chern numbers were computed by integrating the Berry curvature over a sphere of radius 0.01, centered around each Weyl node. Node types and node energies were obtained from the band structure in the vicinity of the nodes.

Coordinates	Node Type	Energy (meV)
[+0.032, -0.179, -0.032]	Type I	-1.5
[+0.043, -0.432, +0.448]	Type I	22.1
[+0.244, -0.127, +0.060]	Type I	-0.5
[-0.127, +0.127, -0.038]	Type I	-3.8
[+0.125, +0.001, -0.003]	Type II	12.2

five inequivalent low-energy Weyl points, which are presented in Table II. Some of these are located above the Fermi energy, and others below, with the closest node only 0.5 meV (6 K) below the Fermi energy.

With the eight symmetry operations of the D_{2d} point group in real space and pure time reversal in momentum space the symmetry transformations generate 16 Weyl nodes for every inequivalent Weyl point. These operations are discussed in Appendix A.

Altogether, this results in a total of $5 \times 16 = 80$ Weyl points, with half carrying Chern number +1 and the other half -1. Not all of them were detected in the DFT+Gutzwiller band structure [18], which could be due to: (i) The more advanced DMFT treatment. Note that the Gutzwiller approximation corresponds to a DMFT approximation to the Gutzwiller wave function [40]. Given that Xu *et al.* [18] found Weyl nodes close to high symmetry lines with e.g. $k_y \approx 0$ it is (ii) also possible that the improved search algorithm used in the present work helped us identify more Weyl points.

Fig. 8 displays the Weyl points in a projection onto $k_z = 0$ and $k_y = 0$ in panels (a) and (b), respectively. Blue and green circles indicate Chern numbers of +1 and -1; overlaid is the projected DMFT spectral functions computed at the Fermi energy. For both the Weyl points and the spectrum, the projections respect the D_{2d} symmetries around the $k_x = k_y$ and $k_x = -k_y$ planes. The density of the Weyl nodes is larger in the vicinity of the Γ point.

In Fig. 9, the dispersion around two exemplary Weyl points of type I and II along the k_y direction is shown at 23 K. For both nodes, the band structure exhibits linearly dispersing crossings close to the Fermi energy, forming Dirac cone-like structures. The Weyl node of type II shown in Fig. 9 (b) is tilted along the (shown) k_y direction. The band crossings of Fig. 9 confirm the presence and topological nature of the identified Weyl points.

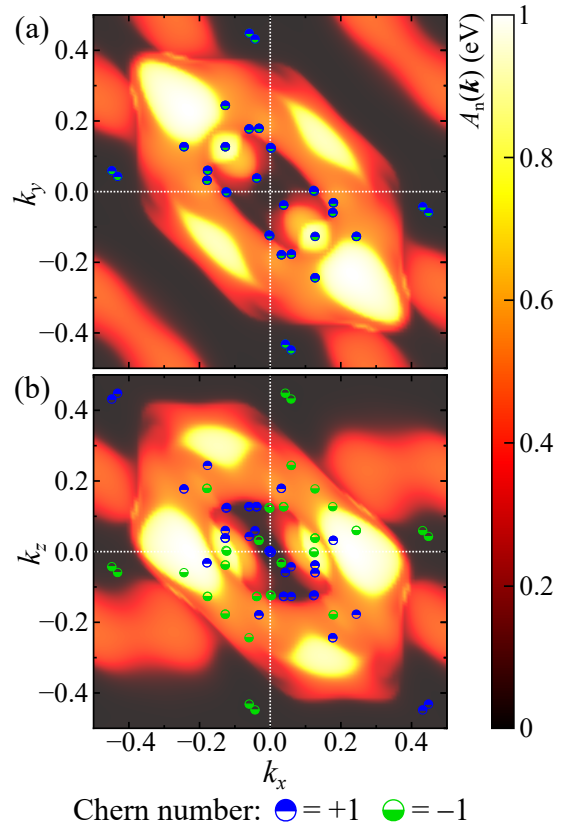


FIG. 8. Projection of the Fermi surface spectral function normalized as $A_n(\mathbf{k}) = A(\mathbf{k}, \omega) / \max(A(\mathbf{k}, \omega))$: (a) in the $[k_x, k_y, 0]$ plane and (b) in the $[k_x, 0, k_z]$ plane. Projected Weyl nodes are marked by blue and green circles, corresponding to the Chern numbers +1 and -1, respectively.

IV. CONCLUSION AND DISCUSSION

We have studied the topology of the low-energy quasi-particle bands of CeRu_4Sn_6 using DFT+DMFT. We find five inequivalent Weyl points or 80 in total at low energies that bridge the Kondo insulator gap induced by the hybridization between $4f$ and conduction electrons. Besides the Kondo temperature which is of the order of 100 K in DMFT, additional energy scales are set by: (i) the size of the direct Kondo gap which is about 5 meV (60K), (ii) the energy range by which the bands above and below this direct Kondo gap cross the Fermi energy which is up to about 1 meV (12K), and last but not least (iii) the distance of the various Weyl points from the Fermi energy, the smallest being 0.5 meV (6 K). Altogether this results in a very complicated situation where different physics sets in with lowering temperature.

Experimentally, an emergent Weyl-Kondo semimetal phase is evidenced in the spontaneous nonlinear Hall effect below 1 K, which is of the same order of magnitude though still considerably lower than the distance of the DMFT Weyl point from the Fermi energy (6 K). While

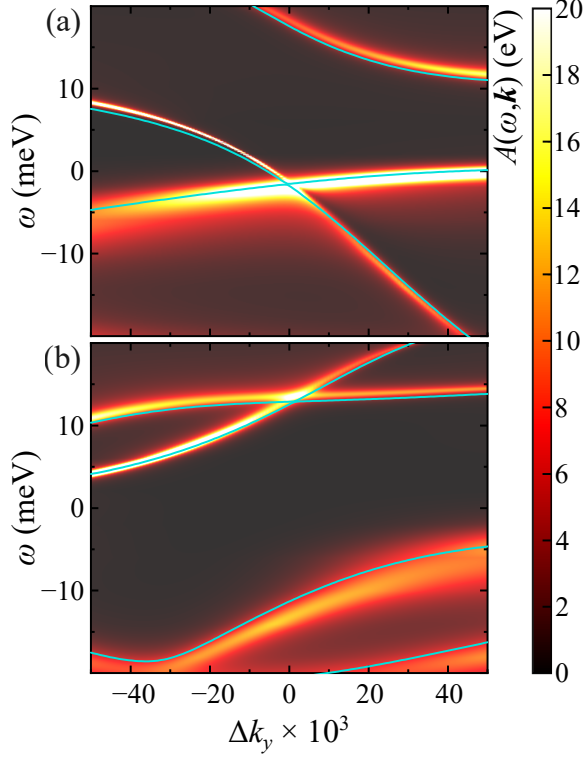


FIG. 9. Quasiparticle bands (lines) and DMFT \mathbf{k} -resolved spectral functions (color overlay) in the vicinity of two selected Weyl nodes: (a) type I node at $[0.032; -0.179; -0.032]$ and (b) type II node at $[0.125; 0.001; -0.003]$. Δk_y is the momentum deviations from the nodes along the k_y direction, while other components are held fixed. [SPB: Does the different intensity/broadness disclose anything about where the bands come from? For instance, does one have a larger $4f$ weight than the other? That would be extremely interesting. Also, does the broadness of the spectral function tell us anything? Could there even be a hint that the width is too large for this to qualify as quasiparticles?]

the Kondo resonance is essentially fully developed at 23 K in DMFT, minor shifts with temperature by less than 1 meV are of course still possible. Also uncertainties in the DFT and DMFT approximations of this magnitude are imaginable.

The ω/T scaling of the inelastic neutron scattering susceptibility further indicates quantum criticality below a scale of 10 K [41]. While quantum criticality and a Kondo breakdown are possible to describe in DMFT, we have no indications for such physics in our calculations which describe a Fermi liquid behavior. However, non-local correlations that are not included in DMFT can compete with the Kondo effect that we capture in DMFT. This competition can alter the physics if with decreasing temperature non-local correlations become strong.

In any case, our theoretical calculations form a firm basis for the understanding of CeRu_4Sn_6 , namely that it is a strongly correlated “failed” Kondo insulator. This

“failure” is twofold: (i) bands above and below the Kondo gap cross the Fermi energy slightly and (ii) Weyl nodes bridge the Kondo gap.

ACKNOWLEDGMENTS

We thank Markus Wallerberger and Andriy Smolyanyuk for very helpful discussions. The support of the Research Unit FOR5249 ‘QUAST’ of the Deutsche Forschungsgemeinschaft [Austrian Science Funds (FWF) project DOI 10.55776/I5868] and the Spezialforschungsbereich (SFB) Q-M&S FWF project DOI 10.55776/F86 is gratefully acknowledged. The computational results have been achieved in part using the Austrian Scientific Computing (ASC) infrastructure. For the purpose of open access, the authors have applied a CC BY-NC-SA public copyright license to any Author Accepted Manuscript version arising from this submission.

Appendix A: D2d symmetry operations in a primitive unit cell

To represent the found Weyl nodes, we have chosen a primitive lattice. In order to convert from this lattice to a conventional lattice, one can change coordinate system by applying a transformation matrix.

The unit vectors for a primitive cell of CeRu_4Sn_6 are (in Å):

$$\begin{aligned} \mathbf{a}_1 &= (-6.502, +6.502, +6.502), \\ \mathbf{a}_2 &= (+6.502, -6.502, +6.502), \\ \mathbf{a}_3 &= (+9.214, +9.214, -9.214). \end{aligned}$$

The corresponding reciprocal lattice vectors are (in \AA^{-1}):

$$\begin{aligned} \mathbf{b}_1 &= (0.000, 0.483, 0.341), \\ \mathbf{b}_2 &= (0.483, 0.000, 0.341), \\ \mathbf{b}_3 &= (0.483, 0.483, 0.000). \end{aligned}$$

The transformation matrix B is constructed by placing the reciprocal vectors as columns:

$$B = \begin{bmatrix} b_{1x} & b_{2x} & b_{3x} \\ b_{1y} & b_{2y} & b_{3y} \\ b_{1z} & b_{2z} & b_{3z} \end{bmatrix} = \begin{bmatrix} 0.000 & 0.483 & 0.483 \\ 0.483 & 0.000 & 0.483 \\ 0.341 & 0.341 & 0.000 \end{bmatrix}$$

To map a node from primitive cell coordinates to conventional cell coordinates, the node’s coordinate vector must be multiplied by B . This transformation yields the coordinates of the Weyl node expressed in the basis of

the conventional reciprocal lattice vectors. It is also possible to go from conventional lattice basis to a primitive one by inverting B .

D_{2d} symmetry operations also take a different form in the primitive cell. To obtain their representation in reciprocal coordinates consistent with the primitive cell, the conventional symmetry matrices α_C can be transformed as follows:

$$\alpha_P = B^{-1} \alpha_C B \quad (\text{A1})$$

This procedure ensures that the symmetry operations act correctly on the reduced \mathbf{k} -space coordinates defined in the primitive basis. Additionally, these transformations are consistent with the changes in the Chern charge associated with the Weyl nodes, ensuring that the symmetry operations correctly map not only the node locations but also their corresponding topological characteristics. All eight D_{2d} symmetry operations in both conventional and primitive cells are summarized in Table III, together with the effects on the Chern charge of the Weyl nodes. Furthermore, time-reversal symmetry relates each Weyl node to a partner with the same Chern charge; its momentum can be obtained by changing the sign of all momentum components. This operation can be combined with the D_{2d} symmetry transformations discussed above, yielding 16 symmetrically related Weyl points in total.

For example, Weyl node $\mathbf{k} = [+0.032, -0.179, -0.032]$ (cf. Table II) with Chern number +1 has 16 symmetry-related replicas (as all other Weyl nodes listed have). Applying e.g. C_{2x} will yield another Weyl node at $\mathbf{k} = [+0.179, -0.032, -0.179]$ (cf. Table III for a primitive cell) with the same Chern number +1. Applying other transformations such as mirror symmetry ($\sigma_{x=y}$) also yield symmetrically related Weyl nodes with opposite Chern number.

TABLE III. D_{2d} symmetry matrices that transform $\mathbf{k} = (k_x, k_y, k_z)^{\text{Tr}}$ on its eight symmetrically related replicas, represented in conventional and primitive reciprocal lattice bases, and transformation effect on the Chern charge.

Symmetry Operation	Conventional Matrix α	Primitive Matrix $B^{-1}\alpha B$	Chern charge
Identity (E)	$\begin{bmatrix} 1 & 0 & 0 \\ 0 & 1 & 0 \\ 0 & 0 & 1 \end{bmatrix}$	$\begin{bmatrix} 1 & 0 & 0 \\ 0 & 1 & 0 \\ 0 & 0 & 1 \end{bmatrix}$	Unchanged
2-fold rotation around x (C_{2x})	$\begin{bmatrix} 1 & 0 & 0 \\ 0 & -1 & 0 \\ 0 & 0 & -1 \end{bmatrix}$	$\begin{bmatrix} -1 & -1 & -1 \\ 0 & 0 & 1 \\ 0 & 1 & 0 \end{bmatrix}$	Unchanged
2-fold rotation around y (C_{2y})	$\begin{bmatrix} -1 & 0 & 0 \\ 0 & 1 & 0 \\ 0 & 0 & -1 \end{bmatrix}$	$\begin{bmatrix} 0 & 0 & 1 \\ -1 & -1 & -1 \\ 1 & 0 & 0 \end{bmatrix}$	Unchanged
2-fold rotation around z (C_{2z})	$\begin{bmatrix} -1 & 0 & 0 \\ 0 & -1 & 0 \\ 0 & 0 & 1 \end{bmatrix}$	$\begin{bmatrix} 0 & 1 & 0 \\ 1 & 0 & 0 \\ -1 & -1 & -1 \end{bmatrix}$	Unchanged
Mirror in $x = y$ plane ($\sigma_{x=y}$)	$\begin{bmatrix} 0 & 1 & 0 \\ 1 & 0 & 0 \\ 0 & 0 & 1 \end{bmatrix}$	$\begin{bmatrix} 0 & 1 & 0 \\ 1 & 0 & 0 \\ 0 & 0 & 1 \end{bmatrix}$	$\mathcal{C} \rightarrow -\mathcal{C}$
Mirror in $x = -y$ plane ($\sigma_{x=-y}$)	$\begin{bmatrix} 0 & -1 & 0 \\ -1 & 0 & 0 \\ 0 & 0 & 1 \end{bmatrix}$	$\begin{bmatrix} 1 & 0 & 0 \\ 0 & 1 & 0 \\ -1 & -1 & -1 \end{bmatrix}$	$\mathcal{C} \rightarrow -\mathcal{C}$
4-fold rotoinversion around z (S_{4z}^+)	$\begin{bmatrix} 0 & 1 & 0 \\ -1 & 0 & 0 \\ 0 & 0 & -1 \end{bmatrix}$	$\begin{bmatrix} -1 & -1 & -1 \\ 0 & 0 & 1 \\ 1 & 0 & 0 \end{bmatrix}$	$\mathcal{C} \rightarrow -\mathcal{C}$
4-fold rotoinversion around z (S_{4z}^-)	$\begin{bmatrix} 0 & -1 & 0 \\ 1 & 0 & 0 \\ 0 & 0 & -1 \end{bmatrix}$	$\begin{bmatrix} 0 & 0 & 1 \\ -1 & -1 & -1 \\ 0 & 1 & 0 \end{bmatrix}$	$\mathcal{C} \rightarrow -\mathcal{C}$

-
- [1] B. Keimer and J. E. Moore, “The physics of quantum materials,” *Nat. Phys.* **13**, 1045 (2017).
- [2] William Witczak-Krempa, Gang Chen, Yong Baek Kim, and Leon Balents, “Correlated quantum phenomena in the strong spin-orbit regime,” *Annu. Rev. Condens. Matter Phys.* **5**, 57 (2014).
- [3] Binghai Yan and Claudia Felser, “Topological materials: Weyl semimetals,” *Annu. Rev. Condens. Matter Phys.* **8**, 337 (2017).
- [4] N. P. Armitage, E. J. Mele, and Ashvin Vishwanath, “Weyl and Dirac semimetals in three-dimensional solids,” *Rev. Mod. Phys.* **90**, 015001 (2018).
- [5] M. G. Vergniory, L. Elcoro, Claudia Felser, Nicolas Regnault, B. Andrei Bernevig, and Zhijun Wang, “A complete catalogue of high-quality topological materials,” *Nature* **566**, 480 (2019).
- [6] Xiaolong Liu and Mark C. Hersam, “2D materials for quantum information science,” *Nat. Rev. Mater.* **4**, 669–684 (2019).
- [7] Kyung-Hwan Jin, Wei Jiang, Gurjyot Sethi, and Feng Liu, “Topological quantum devices: a review,” *Nanoscale* **15**, 12787–12817 (2023).
- [8] Silke Paschen and Qimiao Si, “Quantum phases driven by strong correlations,” *Nat. Rev. Phys.* **3**, 9–26 (2021).
- [9] Joseph G. Checkelsky, B. Andrei Bernevig, Piers Coleman, Qimiao Si, and Silke Paschen, “Flat bands, strange metals, and the Kondo effect,” *Nat. Rev. Mater.* **9**, 509–526 (2024).
- [10] S. Dzsaber, L. Prochaska, A. Sidorenko, G. Eguchi, R. Svagera, M. Waas, A. Prokofiev, Q. Si, and S. Paschen, “Kondo insulator to semimetal transformation tuned by spin-orbit coupling,” *Phys. Rev. Lett.* **118**, 246601 (2017).
- [11] H.-H. Lai, S.E. Grefe, Silke Paschen, and Q. Si, “Weyl-Kondo semimetal in heavy-fermion systems,” *Proc. Natl. Acad. Sci. U.S.A.* **115**, 93 (2018).
- [12] S. Dzsaber, X. Yan, M. Taupin, G. Eguchi, A. Prokofiev, T. Shiroka, P. Blaha, O. Rubel, S.E. Grefe, H.-H. Lai, Q. Si, and S. Paschen, “Giant spontaneous Hall effect in a nonmagnetic Weyl-Kondo semimetal,” *Proc. Natl. Acad. Sci. U.S.A.* **118**, e2013386118 (2021).
- [13] Martin Braß, Jan M. Tomczak, and Karsten Held, “Weyl nodes in $\text{Ce}_3\text{Bi}_4\text{Pd}_3$ revealed by dynamical mean-field theory,” *Phys. Rev. Res.* **6**, 033227 (2024).
- [14] Markus F. Zumdick and Rainer Pöttgen, “Condensed $[\text{Ru}_4\text{Sn}_6]$ units in the stannides LnRu_4Sn_6 ($\text{Ln} = \text{La}, \text{Pr}, \text{Nd}, \text{Sm}, \text{Gd}$) - synthesis, structure, and chemical bonding,” *Z. Naturforsch., B* **54**, 863–869 (1999).
- [15] H. Winkler, K.-A. Lorenzer, A. Prokofiev, and S. Paschen, “Anisotropic electrical resistivity of the Kondo insulator CeRu_4Sn_6 ,” *J. Phys. Conf. Series* **391**, 012077 (2012).
- [16] V. Guritanu, P. Wissgott, T. Weig, H. Winkler, J. Sichelschmidt, M. Scheffler, A. Prokofiev, S. Kimura, T. Iizuka, A.M. Strydom, M. Dressel, F. Steglich, K. Held, and S. Paschen, “Anisotropic optical conductivity of the putative Kondo insulator CeRu_4Sn_6 ,” *Phys. Rev. B* **87**, 115129 (2013).
- [17] E. M. Brünig, M. Baenitz, A. A. Gippius, S. Paschen, A.M. Strydom, and F. Steglich, “ ^{119}Sn solid-state NMR as a local probe for correlations in CeRu_4Sn_6 ,” *Physica B* **378–380**, 839 (2006).
- [18] Yuanfeng Xu, Changming Yue, Hongming Weng, and Xi Dai, “Heavy Weyl fermion state in CeRu_4Sn_6 ,” *Phys. Rev. X* **7**, 011027 (2016).
- [19] Diana M. Kirschbaum, Monika Lužnik, Gwenvredig Le Roy, and Silke Paschen, “How to identify and characterize strongly correlated topological semimetals,” *J. Phys. Mater.* **7**, 012003 (2024).
- [20] D.A. Kirschbaum, L. Chen, D.A. Zocco, H. Hu, F. Mazza, J. Larrea Jiménez, Strydom M.D., D. Adroja, X. Yan, A. Prokofiev, Q. Si, and S. Paschen, “Emergent topological semimetal,” *arXiv:2404.15924* (2024),”.
- [21] Walter Metzner and Dieter Vollhardt, “Correlated Lattice Fermions in $d = \infty$ Dimensions,” *Phys. Rev. Lett.* **62**, 324–327 (1989).
- [22] Antoine Georges and Werner Krauth, “Numerical solution of the $d = \infty$ Hubbard model: Evidence for a Mott transition,” *Phys. Rev. Lett.* **69**, 1240–1243 (1992).
- [23] M Jarrell, “Hubbard model in infinite dimensions: A quantum Monte Carlo study,” *Phys. Rev. Lett.* **69**, 168–171 (1992).
- [24] Antoine Georges, Gabriel Kotliar, Werner Krauth, and Marcelo J Rozenberg, “Dynamical mean-field theory of strongly correlated fermion systems and the limit of infinite dimensions,” *Rev. Mod. Phys.* **68**, 13 (1996).
- [25] Eva Pavarini, Erik Koch, Dieter Vollhardt, and Alexander Lichtenstein, *DMFT at 25: Infinite Dimensions* (Forschungszentrum Jülich, 2014) modeling and Simulation Vol. 4.
- [26] V I Anisimov, A I Poteryaev, M A Korotin, A O Anokhin, and G Kotliar, “First-principles calculations of the electronic structure and spectra of strongly correlated systems: dynamical mean-field theory,” *Journal of Physics: Condensed Matter* **9**, 7359–7367 (1997).
- [27] A I Lichtenstein and M I Katsnelson, “Ab initio calculations of quasiparticle band structure in correlated systems: LDA++ approach,” *Phys. Rev. B* **57**, 6884–6895 (1998).
- [28] K Held, “Electronic structure calculations using dynamical mean field theory,” *Adv. Phys.* **56**, 829–926 (2007).
- [29] Klaus Koepernik and Helmut Eschrig, “Full-potential nonorthogonal local-orbital minimum-basis band-structure scheme,” *Phys. Rev. B* **59**, 1743–1757 (1999).
- [30] Peter Blaha, Karlheinz Schwarz, Fabien Tran, Robert Laskowski, Georg K. H. Madsen, and Laurence D. Marks, “WIEN2k: An APW+lo program for calculating the properties of solids,” *J. Chem. Phys.* **152**, 074101 (2020).
- [31] Philipp Wissgott, *Transport Properties of Correlated Materials from First Principles*, Ph.D. thesis, Technische Universität Wien (2012).
- [32] John P. Perdew and Yue Wang, “Accurate and simple analytic representation of the electron-gas correlation energy,” *Phys. Rev. B* **45**, 13244–13249 (1992).
- [33] Markus Wallerberger, Andreas Hausoel, Patrik Gunnacker, Alexander Kowalski, Nicolaus Parragh, Florian Goth, Karsten Held, and Giorgio Sangiovanni, “w2dynamics: Local one- and two-particle quantities from dynamical mean field theory,” *Comput. Phys. Commun.* **235**, 388–399 (2019).
- [34] Emanuel Gull, Andrew J. Millis, Alexander I. Licht-

- enstein, Alexey N. Rubtsov, Matthias Troyer, and Philipp Werner, “Continuous-time Monte Carlo methods for quantum impurity models,” *Rev. Mod. Phys.* **83**, 349–404 (2011).
- [35] Vladimir I Anisimov, Jan Zaanen, and Ole K Andersen, “Band theory and Mott insulators: Hubbard U instead of Stoner I ,” *Phys. Rev. B* **44**, 943 (1991).
- [36] Josef Kaufmann and Karsten Held, “ana_cont: Python package for analytic continuation,” *Comput. Phys. Commun.* **282**, 108519 (2023).
- [37] S. Ali Hassani Gangaraj, Mario G. Silveirinha, and George W. Hanson, “Berry phase, Berry connection, and Chern number for a continuum bianisotropic material from a classical electromagnetics perspective,” *IEEE J. Multiscale Multiphys. Comput. Tech.* **2**, 3–17 (2017).
- [38] Martin Braß, Liang Si, and Karsten Held, “Weyl points and spin-orbit coupling in copper-substituted lead phosphate apatite,” *Phys. Rev. B* **109**, 085103 (2024).
- [39] Martin Sundermann, Fabio Strigari, Thomas Willers, Hannes Winkler, Andrey Prokofiev, James M. Ablett, Jean-Pascal Rueff, Detlef Schmitz, Eugen Weschke, Marco Moretti Sala, Ali Al-Zein, Arata Tanaka, Maurits W. Haverkort, Deepa Kasinathan, Liu Hao Tjeng, Silke Paschen, and Andrea Severing, “CeRu₄Sn₆: a strongly correlated material with nontrivial topology,” *Sci. Rep.* **5** (2015), 10.1038/srep17937.
- [40] See Chapter 1 of [25].
- [41] Wesley T. Fuhrman, Andrey Sidorenko, Jonathan Hänel, Hannes Winkler, Andrey Prokofiev, Jose A. Rodriguez-Rivera, Yiming Qiu, Peter Blaha, Qimiao Si, Collin L. Broholm, and Silke Paschen, “Pristine quantum criticality in a Kondo semimetal,” *Sci. Adv.* **7**, eabf9134 (2021).